OPEN

Free-standing Fe_2O_3 nanomembranes enabling ultra-long cycling life and high rate capability for Li-ion batteries

Xianghong Liu[1], Wenping Si[1,2], Jun Zhang[4], Xiaolei Sun[1,2], Junwen Deng[1,2], Stefan Baunack[1], Steffen Oswald[5], Lifeng Liu[6], Chenglin Yan[1,3] & Oliver G. Schmidt[1,2]

[1]Institute for Integrative Nanosciences, IFW-Dresden, Helmholtzstrasse 20, 01069 Dresden, Germany, [2]Material Systems for Nanoelectronics, Chemnitz University of Technology, Reichenhainerstrasse 70, 09107 Chemnitz, Germany, [3]College of Physics, Optoelectronics and Energy & Collaborative Innovation Center of Suzhou Nano Science and Technology, Soochow University, 215006 Suzhou, China, [4]School of Materials Science and Engineering, University of Jinan, 250022 Jinan, China, [5]Institute for Complex Materials, IFW-Dresden, Helmholtzstrasse 20, 01069 Dresden, Germany, [6]International Iberian Nanotechnology Laboratory (INL), Avenida Mestre José Veiga s/n, 4715-330, Braga, Portugal.

With Fe_2O_3 as a proof-of-concept, free-standing nanomembrane structure is demonstrated to be highly advantageous to improve the performance of Li-ion batteries. The Fe_2O_3 nanomembrane electrodes exhibit ultra-long cycling life at high current rates with satisfactory capacity (808 mAh g^{-1} after 1000 cycles at 2 C and 530 mAh g^{-1} after 3000 cycles at 6 C) as well as repeatable high rate capability up to 50 C. The excellent performance benefits particularly from the unique structural advantages of the nanomembranes. The mechanical feature can buffer the strain of lithiation/delithiation to postpone the pulverization. The two-dimensional transport pathways in between the nanomembranes can promote the pseudo-capacitive type storage. The parallel-laid nanomembranes, which are coated by polymeric gel-like film and SEI layer with the electrolyte in between layers, electrochemically behave like numerous "mini-capacitors" to provide the pseudo-capacitance thus maintain the capacity at high rate.

Two dimensional (2D) inorganic nanomembranes have lateral dimension at least two orders of magnitude larger than the thickness[1,2], and can well combine the merits of the 0D and 1D counterparts[3]. With the unique mechanical feature, the 2D nanomembranes can be distorted, wrinkled and folded into 3D configurations, such as rolled-up, wavy and helical structures[2–5]. The mechanical feature is rather attractive and particularly expected to buffer the strain of lithiation/delithiation for the applications in lithium-ion batteries (LIBs)[6,7]. The special electronic structure on the surface also makes the nanomembranes quite suitable for applications in electronic and energy devices[2,8]. The nanomembranes can provide two dimensional transport pathways in between the layers, which can promote the pseudo-capacitive type storage of the electrode[9].

Rechargeable LIBs have now become the dominant energy storage devices in portable electronics and also show great potential in hybrid electric vehicles[10–13]. To meet the increasing demands for high performance batteries, electrode materials with high energy and power density, long cycling life, low cost and safety are highly required. Possessing advantages of high theoretical capacity ($\sim$1005 mAh g^{-1}), good stability, low cost, abundance in nature, and environmental benignity[14], Fe_2O_3 is therefore a promising conversion-type transition metal oxide anode material. Nanoarchitecture shows great potential in improving the battery performance as a result of the large interfacial contact at the electrode/electrolyte interface and the nanosized diffusion paths for Li$^{+13–16}$. Various Fe_2O_3 nanostructures such as nanorods[17], nanotubes[18], microboxes[19], multi-shelled hollow microspheres[20], hierarchical hollow spheres[21], as well as the composites with C-based material[22–24], have been designed to obtain high performance. However, the commercialization of Fe_2O_3 anodes for LIBs is still limited by the unsatisfactory capacity retention with short cycling life due to the pulverization upon repeated volume expansion/extraction. Therefore, there are still great challenges to achieve long cycling life for thousands of cycles and high rate capability with satisfactory reversible capacity for high power applications.

In this contribution, with Fe_2O_3 as a proof-of-concept, free-standing nanomembranes are designed to investigate the effect of nanomembrane structure on the electrochemical performance for LIBs. The Fe_2O_3 nanomembrane electrodes exhibit very encouraging results with ultra-long cycling life and high rate capability.

Results

Material Characterization. The morphology of the samples was observed by scanning electron microscopy (SEM). The original Fe nanomembranes have a lateral size of tens to hundreds of microns and are composed of numerous tiny nanoparticles (Supplementary Fig. S1). Some of the nanomembranes bend up induced by the built-in differential stress[2,4]. The Fe nanomembranes were converted into Fe_2O_3 nanomembranes by annealing oxidation in air. The obtained Fe_2O_3 nanomembranes still well preserve the similar layer structure and the nanoparticles-stacked rough surface (Fig. 1a and 1b). For the thickness measurements, focused ion beam (FIB) etching was performed with a single Fe_2O_3 nanomembrane. The cross section image (inset of Fig. 1b) reveals the thickness of a Fe_2O_3 nanomembrane to be about 103 ∼ 165 nm.

The crystallographic structure and phase of the Fe_2O_3 nanomembranes were analyzed by powder X-ray diffraction (XRD). As shown in Fig. 1c, most of the diffraction peaks are well indexed to rhombohedral hematite $\alpha\text{-}Fe_2O_3$ (JCPDS no. 33-0664) and the minor peak at $2\theta = 35.3°$ is attributed to tetragonal maghemite $\gamma\text{-}Fe_2O_3$ (JCPDS no. 25-1402). The $\gamma\text{-}Fe_2O_3$ nanophase should originate from the

passive film on the surface of Fe nanomembranes. The passive film is caused by the alkaline corrosion of hydroxyl ions and/or oxygen and has complicated composition including a series of iron oxides (Fe_3O_4 or $\gamma\text{-}Fe_2O_3$) and/or oxyhydroxides (α, β, $\gamma\text{-}FeOOH$)[25–27].

The Raman spectrum (Supplementary Fig. S2a) exhibits two A_{1g} modes at about 229 and 501 cm^{-1}, three E_{1g} symmetry modes at about 295, 415, and 615 cm^{-1}, and a $2E_u$ mode at ~ 1320 cm^{-1} [28], which are the typical Raman modes of crystalline $\alpha\text{-}Fe_2O_3$. However, the $\gamma\text{-}Fe_2O_3$ nanophase only exhibits a weak broad peak at ~ 1532 cm^{-1} [29], which may be because of the weak peak intensity of $\gamma\text{-}Fe_2O_3$[30], or the phase transformation of partial $\gamma\text{-}Fe_2O_3$ into $\alpha\text{-}Fe_2O_3$ under laser radiation during Raman testing[31]. The surface composition and valence states of the nanomembranes were determined by X-ray photoelectron spectroscopy (XPS). The Fe 2p XPS spectrum (Supplementary Fig. S2b) exhibits the typical XPS feature of Fe 2p (III) which shows the signals of Fe 2p$_{1/2}$ and Fe 2p$_{3/2}$ at the binding energies of 713.2 and 726.7 eV with their corresponding satellite peaks at 721.1 and 735.6 eV arising from the charge transfer screening[32]. Only very weak 'ghost' peak can be seen in the Al 2p XPS spectrum region (Supplementary Fig. S2c), and it is hard to be
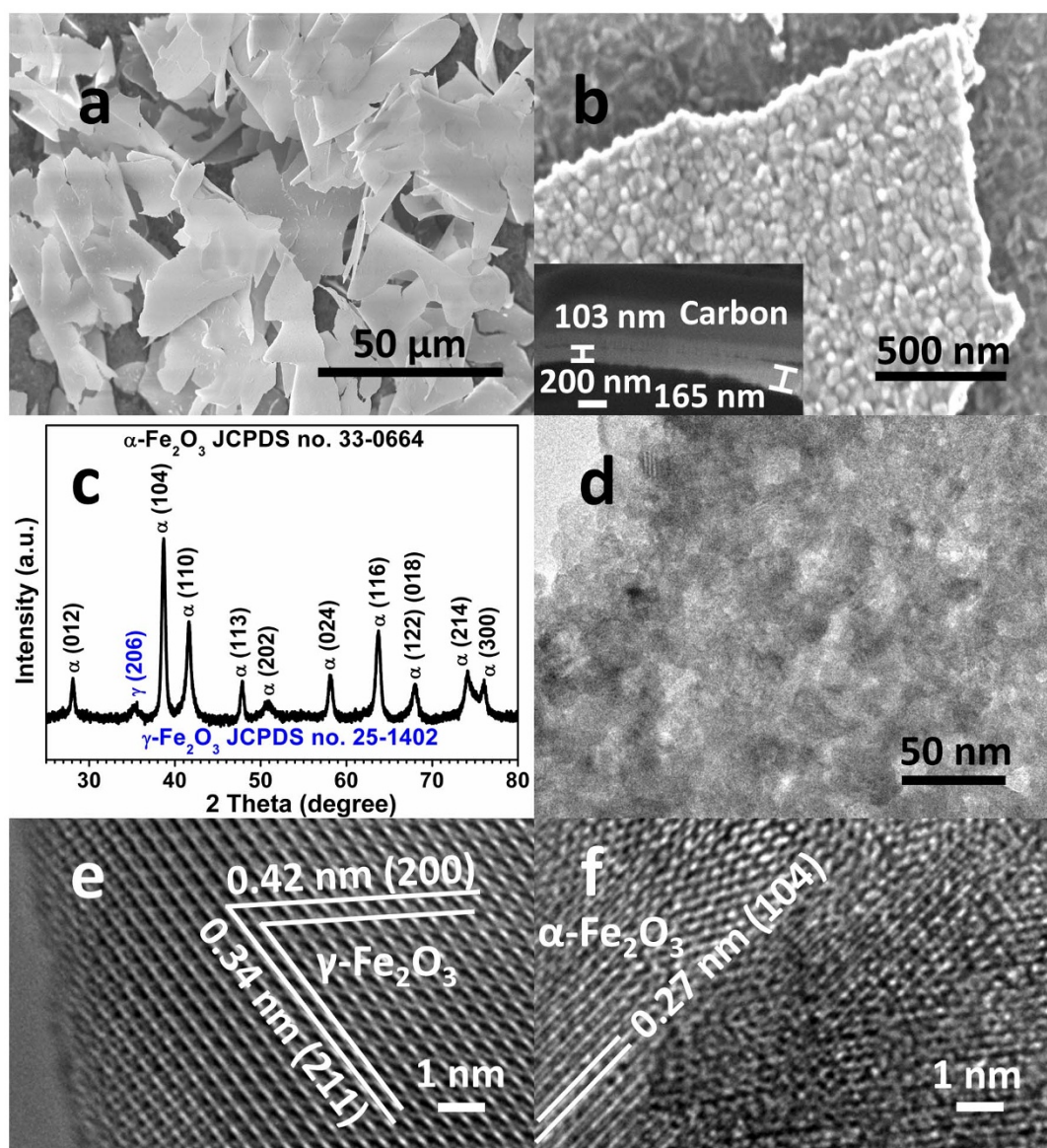

Figure 1 | Characterizations of the Fe_2O_3 nanomembranes. (a) low and (b) high magnification SEM images (inset of (b): cross-section image from FIB cutting of a nanomembrane), (c) XRD pattern, (d) TEM image, and (e–f) HR-TEM images of $\gamma\text{-}Fe_2O_3$ and $\alpha\text{-}Fe_2O_3$ nanophase.

assigned to Al 2p or noise signal. No signals of other species can be detected in the wide spectrum (Supplementary Fig. S2d), implying the high purity of the sample.

Transmission electron microscopy (TEM) analysis was performed to characterize the microstructure and composition of the Fe_2O_3 nanomembranes. The rough structure of the nanomembrane can be seen from the different contrast of the TEM image in Fig. 1d, which is consistent with the SEM observation (Fig. 1b). High-resolution TEM (HR-TEM) images are taken to differentiate the γ-Fe_2O_3 and α-Fe_2O_3 nanophases in the Fe_2O_3 nanomembranes. The two series of uniform lattice spacings of 0.34 nm and 0.42 nm marked in Fig. 1e can be well indexed to the spacings of the (211) and (200) planes of γ-Fe_2O_3, respectively. The lattice spacing of 0.27 nm marked in Fig. 1f corresponds to the (104) plane of α-Fe_2O_3. The HR-TEM results are in good agreement with the above mentioned XRD pattern and Raman analysis.

Electrochemical Performance. The Fe_2O_3 nanomembranes were electrochemically evaluated by cyclic voltammetry (CV), galvanostatic discharge/charge cycling and electrochemical impedance spectra (EIS) with two-electrode Swagelok-type half-cells. Regardless of the α-Fe_2O_3 or γ-Fe_2O_3 nanophases, the electrochemical behavior of Fe_2O_3 follows the conversion reaction mechanism of $Fe_2O_3 + 6Li^+ + 6e^- \leftrightarrow 2Fe + 3Li_2O$[11,14]. The initial five CV curves of the Fe_2O_3 nanomembrane electrode are displayed in Fig. 2a. The first discharge process exhibits three peaks related to the different reaction stages. The minor peak at ~1.64 V (inset of Fig. 2a) corresponds to the initial lithiation of Fe_2O_3 to form $Li_xFe_2O_3$ (Equation (1) and (2))[33]. The minor shoulder peak at ~0.9 V (inset of Fig. 2a), which is overlapped by the following sharp cathodic peak, is related to the phase change from hexagonal α-$Li_xFe_2O_3$ to cubic $Li_2Fe_2O_3$ with further Li uptake (Equation (3))[33]. The reason why the phase transition peak is unobvious should be the fact that the Fe_2O_3 nanomembranes consist of α-Fe_2O_3/γ-Fe_2O_3 mixed phase and 1 mol γ-Fe_2O_3 nanoparticles can intake up to 1.37 mol lithium (x=1.37 in $Li_xFe_2O_3$) without phase change[34]. The sharp cathodic peak at ~0.59 V is caused by the reduction of Fe(III) to Fe (Equation (4)), the formation of solid electrolyte interphase (SEI) layer, and the decomposition of the kinetically activated electrolyte by Fe nanoparticles to form polymeric gel-like film in the low-voltage[33,35]. In the subsequent charging process, the two broad overlapped anodic peaks at ~1.61 and ~1.84 V are associated with the reversible multistep oxidation of Fe to FeO and then to Fe_2O_3[36].

After the reduction reaction in the first discharge process, the crystallinity of the Fe_2O_3 nanomembranes is destroyed and can't be regained during the subsequent charge process[36], therefore, afterwards the Fe_2O_3 electrode behaves electrochemically as amorphous Fe_2O_3. In the 2nd cycle, the peak for the partial lithiation of Fe_2O_3 to $Li_xFe_2O_3$ (Equation (1)) shifts to ~1.18 V (disappears in the 5th cycle) and the main cathodic peak for the reduction of Fe(III) to Fe shifts to ~0.95 V, which also agrees well with the profile of amorphous Fe_2O_3[37]. The shoulder peak at ~0.84 V in the 2nd cycle (shifts to ~0.60 V in the subsequent cycles) should arise from the further decomposition of electrolyte and formation of SEI layer at the low voltage. The absence of the above mentioned minor cathodic peak at ~0.9 V in the subsequent cycles confirms the irreversible phase change from hexagonal α-$Li_xFe_2O_3$ to cubic $Li_2Fe_2O_3$[22].

$$Fe_2O_3 + xLi^+ + xe^- \rightarrow Li_xFe_2O_3 \quad (1)$$

$$\alpha - Fe_2O_3 + xLi^+ + xe^- \rightarrow \alpha - Li_xFe_2O_3 \ (hexagonal) \quad (2)$$

$$\alpha - Li_xFe_2O_3 + (2-x)Li^+ + (2-x)e^- \rightarrow Li_2Fe_2O_3 (cubic) \quad (3)$$

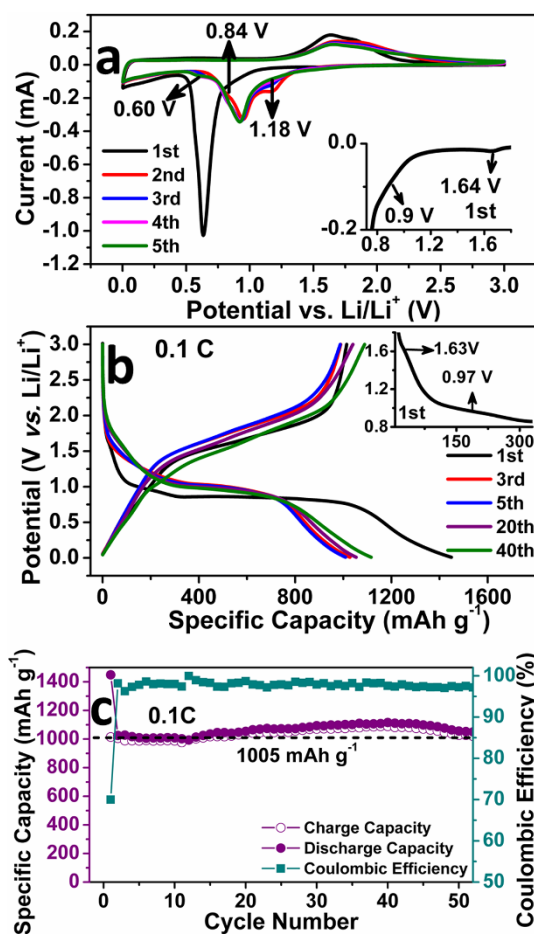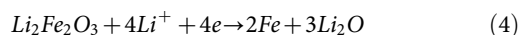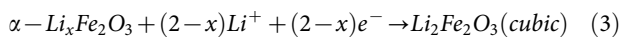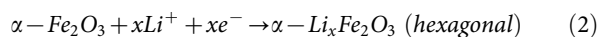$$Li_2Fe_2O_3 + 4Li^+ + 4e^- \rightarrow 2Fe + 3Li_2O \quad (4)$$

Figure 2 | Electrochemical properties of the Fe_2O_3 nanomembrane electrodes. (a) CV curves (inset: enlarged part of the 1st discharge), (b) Representative galvanostatic discharge/charge voltage curves at 0.1 C (inset: enlarged part of the 1st discharge), (c) Discharge/charge cycling performance at 0.1 C.

The representative discharge/charge voltage curves at the current density of 0.1 C (1 C = 1005 mA g^{-1}) in Fig. 2b agree well with the CV result. The first discharge process includes four regions corresponding to the different reaction stages. The minor slope at ~1.63 V (inset of Fig. 2b) arises from the initial lithiation of Fe_2O_3 nanomembranes to form $Li_xFe_2O_3$ (Equation (1) and (2)), offering a capacity of ~24 mAh g^{-1} with the Li uptake of ~x=0.14 in $Li_xFe_2O_3$. The minor slope at ~0.97 V (inset of Fig. 2b) is ascribed to the phase transition from hexagonal α-$Li_xFe_2O_3$ to cubic $Li_2Fe_2O_3$ upon further lithiation. The obvious broad plateau around 0.85 V is assigned to the reduction of Fe(III) to Fe. The slope after 0.8 V is related to the SEI layer formation and the decomposition of electrolyte to form polymeric gel-like film in the low-voltage[33].

The cycling performance of the Fe_2O_3 nanomembrane electrode at 0.1 C is shown in Fig. 2c. The electrode delivers an initial discharge/charge capacity of 1449/1014 mAh g^{-1} with the coulombic efficiency of 70%. After the slight decrease in the subsequent several cycles, the capacity increases gradually and keeps a stable cycling. The reversible capacity after 52 cycles is 1020 mAh g^{-1} (coulombic efficiency: 97%), which is still beyond the theoretical capacity of Fe_2O_3. The capacity after cycling beyond the theoretical capacity was also reported in the publication with much higher capacity of 1600 mAh g^{-1} at 1 C after 500 cycles on the amorphous Fe_2O_3 film anode[37]. This can be interpreted by the interfacial storage at the interfaces of solid-electrolyte and solid-solid, including the surface storage via charge separation at the interface of Fe and Li_2O nanograins[38,39], the storage of Li-contain-
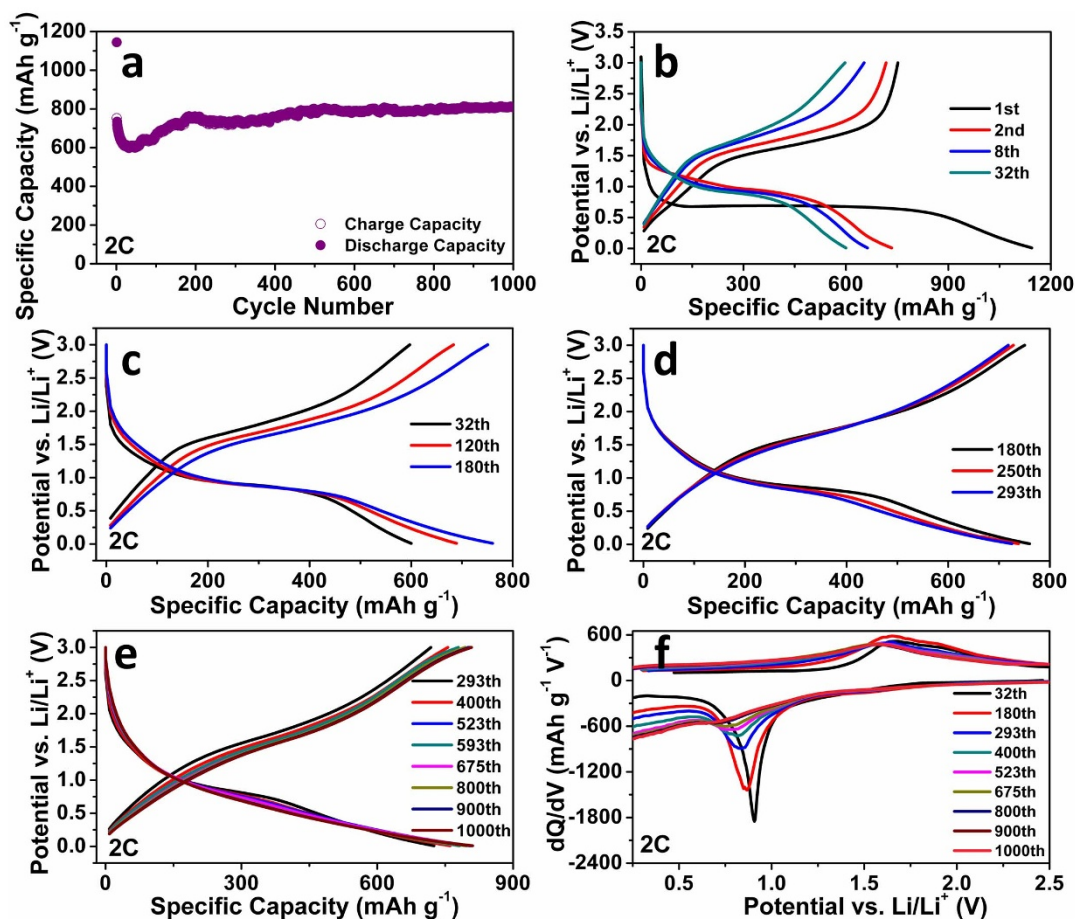
Figure 3 | Cycling performance of the Fe₂O₃ nanomembrane electrode at 2 C. (a) discharge/charge cycling performance, (b–e) corresponding representative discharge/charge voltage curves and (f) differential specific capacity versus voltage plots.

ing SEI layer[40], and the pseudo-capacitive type storage of the reversibly formed polymeric gel-like film at low voltage[35]. A solid state NMR study proposes that the reversible reaction of LiOH (formed from the surface OH of metal oxide) with Li to form Li_2O and LiH is also a source of the excess capacity[41]. As for the capacity increase after initial decrease, some reference addressed it as the activation process of the electrode materials, but the detailed mechanism is still not fully revealed. Figure 2b exhibits the representative discharge/charge voltage curves at 0.1 C. Except for the first cycle, the profile of the discharge/charge voltage curves of the subsequent cycles is similar and featured with shortened plateau and slightly increased plateau potential. However, from the 5th to 40th cycle, the capacity increase slightly in the low-voltage slope region (< 0.8 V) with a capacity increment of 120 mAh g^{-1}. The capacity increase at low voltage region (< 0.8 V) indicates the pseudo-capacitive type storage, especially from the polymeric gel-like film[35].

Figure 3a shows the cycling performance of the Fe₂O₃ nanomembrane electrode at 2 C with the initial discharge/charge capacity of 1144/752 mAh g^{-1}. In the first 32 cycles, the capacity decays slowly because of the further formation of SEI layer. Then the electrode keeps a very long and stable cycling with a reversible capacity of 808 mAh g^{-1} (coulombic efficiency: 99.7%) after 1000 cycles. The corresponding representative discharge/charge voltage curves in Fig. 3b–e clearly reveal the capacity variation at the different stages of the long cycling. The capacity decreases in the reduction (quasi-)plateau region and increases in the low-voltage slope region (<0.8 V). The decreased contribution from the reduction/oxidation reaction of Fe(III)↔Fe(0) to the capacity can be seen from the gradually weakened reduction (quasi-)plateaus (Fig. 3b–e) and the nega-

tively-shifted cathodic peaks (Fig. 3f). Upon further cycling, the thickened SEI layer hinders the diffusion of Li$^+$ into the inner part of the electrode material especially at fast discharge/charge rate. Under the difficult solid-state diffusion, the interfacial storage, especially the pseudo-capacitive type storage, will be obvious to maintain the capacity[9]. That's why the Fe₂O₃ nanomembrane electrode can keep a long stable cycling with satisfactory capacity under the decreased contribution from the reduction/oxidation reaction.

The electrochemical impedance spectra (EIS) were measured to analyze the variation of impedance and diffusion in the Fe₂O₃ nanomembrane electrode before and after cycling at 2 C. In the high frequency region (inset of Fig. 4a and 4b), the semicircle diameter of the Nyquist plots after cycling at both the fixed potential of 3.0 V and open circuit potential (OCP) decreases greatly than that before cycling. The decreased semicircle diameter implies the reduced charge transfer resistance[17]. Upon cycling, because of the increased ohmic resistance such as active material resistance and SEI resistance[42], the transition from the Warburg-type semi-infinite linear diffusion (45° fitting line) to quasi finite diffusion (fitting line approaching 90°) in the Nyquist plots at 3.0 V (Fig. 4a) is shifted to the lower frequency region, which reveals the decreased solid-state diffusion coefficient[43–45]. The Warburg coefficient, defined as the slope of the fitting line of the relationship between Z′ and $\omega^{-1/2}$ within 10~1 Hz (Fig. 4c)[46], increases upon cycling, indicating the increased Warburg impedance. However, the slope of the 500th cycle decreases slightly than that of the 200th one, and the reason for this should be the cracking of the nanomembranes with new interfaces exposed for storage. In very low frequency region, the steeper slopes of the fitting Nyquist plots at OCP (Fig. 4b) after further cycling
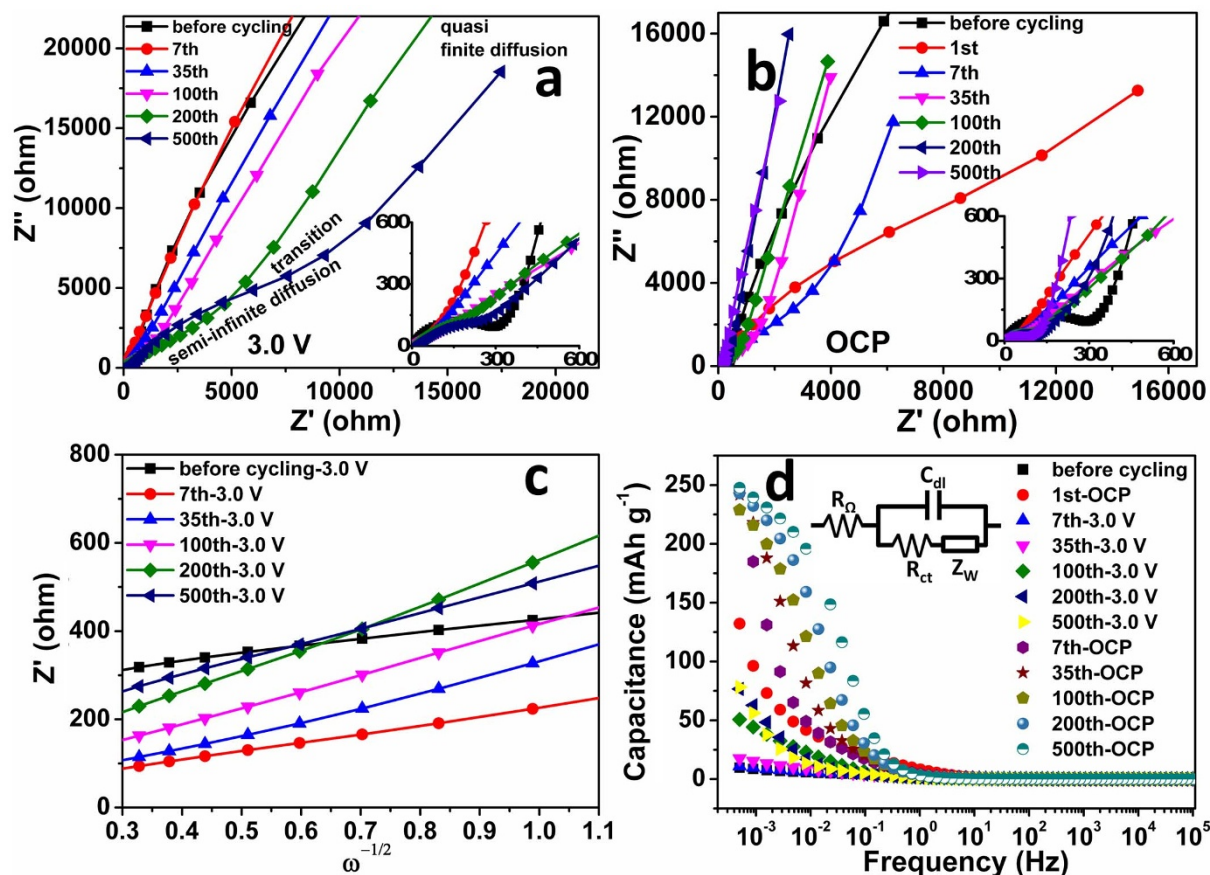
Figure 4 | EIS of the Fe$_2$O$_3$ nanomembrane electrode before and after cycling at 2 C. Nyquist plots (inset: enlarged part of the high frequency region) at (a) fixed potential of 3.0 V and (b) OCP, (c) the relationship between Z' and $\omega^{-1/2}$ within 10 ~ 1 Hz, and (d) real part of the capacitance $C'(\omega)$ *versus* frequency before and after cycling at 2 C within 10^5 ~ 5×10^{-4} Hz. Inset of (d) is the simplified electrochemical system as Randles circuit (R$_\Omega$: ohmic resistance, C$_{dl}$: double-layer capacitance, R$_{ct}$: charge transfer resistance, and Z$_W$: Warburg impedance). (symbols: real data, lines: fitting curves).

imply the more obvious pseudo-capacitive behavior of the electrode[35]. The real part of the capacitance $C'(\omega)$, corresponding to the capacitance of the cell measured during constant current discharge, can be obtained from Equation (5)[47,48].

$$C'(\omega) = \frac{-Z''(\omega)}{\omega|Z(\omega)|^2} \tag{5}$$

The capacitance $C'(\omega)$ versus frequency obtained from EIS at both OCP and 3.0 V is shown in Fig. 4d. The OCP capacitance should mainly originate from the incompletely decomposed polymeric gel-like film at fast charge rate[35]. Within 1.46×10^{-1}~1.57×10^{-3} Hz, the increase of OCP capacitance shifts to higher frequency upon cycling, which agrees with the steeper tendency of the Nyquist plots at OCP. The OCP capacitance at 500 μHz is 132 mAh g^{-1} (calculated based on the total weight of the active material) after the 1st cycle and increases to 264 mAh g^{-1} after 7 cycles, and then fluctuates slightly in the subsequent cycles, which however doesn't show a regular change. This fluctuation probably arises from the different decomposition degree of the polymeric gel-like film at different OCP after different cycles. The capacitance $C'(\omega)$ of 3.0 V at 500 μHz increases with the cycle number increasing until 200 cycles, however, it is only 76 mAh g^{-1} after 200 cycles and much less than that of OCP. Since the low-potential (0.02 ~ 1.8 V) existent polymeric gel-like film disappears after being fully charged to the fixed potential of 3.0 V[35], the capacitance obtained at 3.0 V may be caused by the gradually thickened SEI layer as it increases with the cycle number increasing. The capacitance of the SEI layer may be one of the reasons for the capacity increase after the initial decrease. However, the capacitance of 3.0 V at 500 μHz doesn't always increase when the SEI

layer becomes thicker, and too much thicker SEI layer will lead to the decreased capacitance. After 500 cycles, the capacitance of 3.0 V at 500 μHz is only 78 mAh g^{-1} which is close to that after 200 cycles, while it decreases slightly instead of increasing within 0.03 ~ 0.004 Hz.

The current density was increased to a high rate of 6 C to further investigate the cycling performance of the Fe$_2$O$_3$ nanomembrane electrode. Figure 5a shows the ultra-long cycling performance at 6 C for 3000 cycles (the initial 100 cycles at 1 C) and the comparison with the theoretical capacity of graphite. The initial discharge/charge capacity at 1 C is 1232/803 mAh g^{-1} and the reversible capacity of the 100th cycle at 1 C is 834 mAh g^{-1} (coulombic efficiency: 98.9%). When the current density increases to 6 C, the first discharge/charge capacity is 715/610 mAh g^{-1}. Then the electrode keeps an ultra-long and stable cycling at 6 C with reversible capacity of ~570 ± 40 mAh g^{-1} (coulombic efficiency: 99.5% ~ 100%). The reversible capacity of 530 mAh g^{-1} after 3000 cycles is still much higher than the theoretical capacity of graphite. The gradually weakened reduction/oxidation (quasi-)plateaus (Supplementary Fig. S3a) and cathodic/anodic peaks (Supplementary Fig. S3b) indicate the decreased capacity contribution from the reduction/oxidation reaction. At such a high rate of 6 C with more difficult diffusion inwards the electrode material, the pseudo-capacitance becomes more prominent and plays a particularly important role in the ultra-long cycling under the fast surface kinetics.

The rate capability of the Fe$_2$O$_3$ nanomembrane electrode was examined by a stepwise current density discharge/charge program. As shown in Fig. 5b, two turns of rate capability measurements are collected at various current rates from 0.2 C to 50 C. The initial
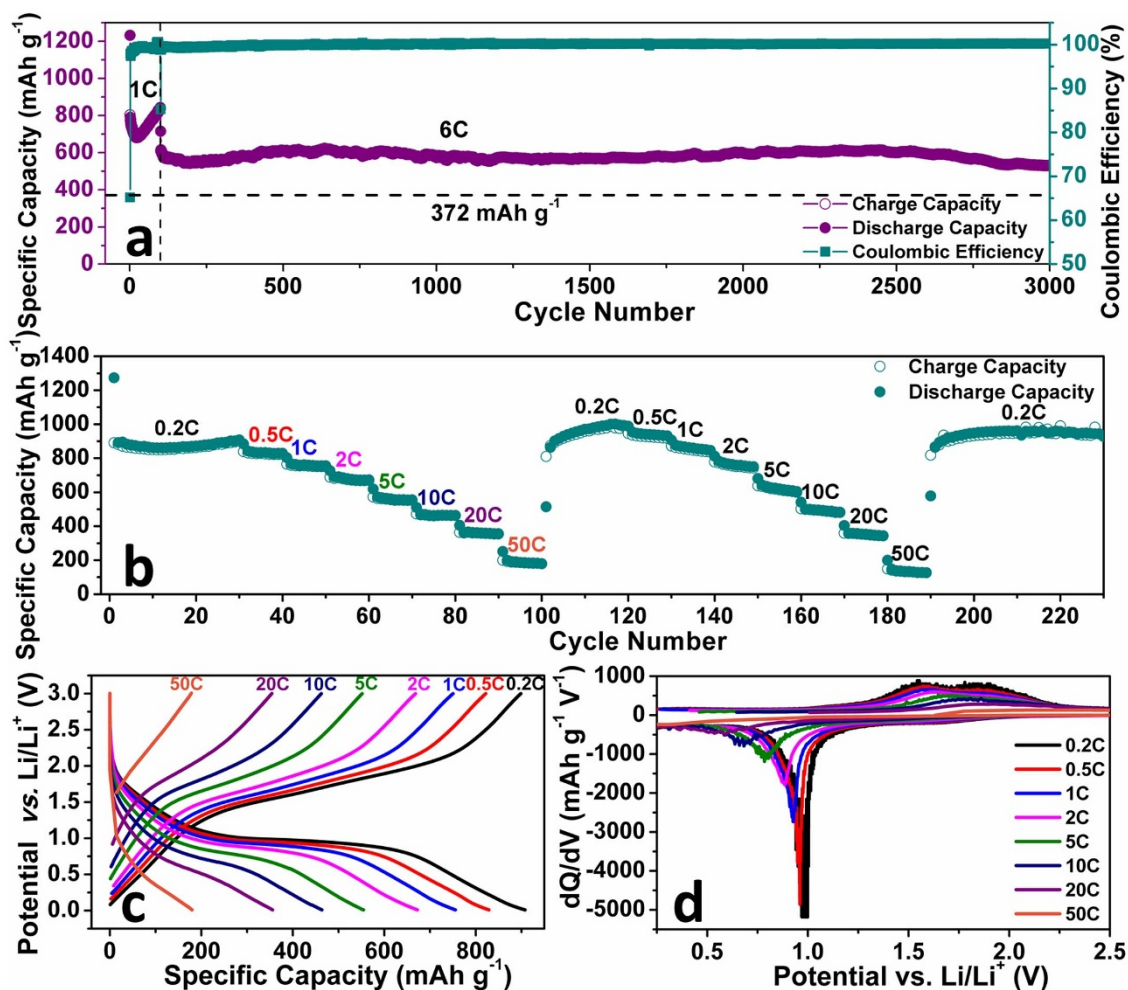
Figure 5 | Electrochemical performance of the Fe$_2$O$_3$ nanomembrane electrodes. (a) discharge/charge cycling performance at 6 C (initial 100 cycles at 1 C), (b) Rate capability, (c) corresponding representative discharge/charge voltage curves and (d) differential specific capacity versus voltage plots at various C-rates.

discharge/charge capacity at 0.2 C is 1294/891 mAh g^{-1} and the reversible capacity after 30 cycles is 899 mAh g^{-1}. The capacity decreases with the current rate increasing from 0.2 C to an extremely high rate of 50 C. Although there is hysteresis in the first discharge capacity of each rate due to the diffusion hysteresis, stable capacities could be quickly retained during the subsequent cycles at each rate. The reversible capacity of the last cycle at 0.5 C, 1 C, 2 C, 5 C, 10 C, 20 C, and 50 C in the first turn is 822, 750, 668, 552, 462, 354, and 178 mAh g^{-1}, respectively. When the current rate was dramatically set back to 0.2 C from 50 C, a reversible capacity of 946 mAh g^{-1} (the 120th cycle) can still be obtained. Impressively, when successively subjected to the second turn of rate capability measurement, the Fe$_2$O$_3$ nanomembrane electrode exhibits excellent capacity retention with almost the similar capacity in the first turn, demonstrating the repeatable high rate capability. Even after two turns of rate capability measurements up to 50 C, the electrode can still keep a stable cycling at 0.2 C with the reversible capacity of 927 mAh g^{-1} after 230 cycles, which indicates the good stability and reversibility of the Fe$_2$O$_3$ nanommebrane electrode.

Figure 5c and 5d respectively shows the representative discharge/charge voltage curves and their corresponding differential specific capacity versus voltage plots of the last cycle at various rates in the first turn of rate capability measurement. Although the charge voltage curve of 50 C nearly becomes a straight line at such a fast cycling rate, the profile of the voltage curves from 0.2 C to 20 C exhibits a similar shape. With the current rate increasing, the overpotential becomes higher with the lower discharge and higher charge potential of the plateaus (or slopes) (Fig. 5c); the electrode polarization also becomes more severe with the negatively-shifted cathodic peaks and the positively-shifted anodic peaks (Fig. 5d). The higher overpotential and the severe polarization indicates that the reduction/oxidation reaction proceeds more difficultly at much higher rates, as confirmed by the weakened reduction/oxidation plateaus (or slopes) and cathodic/anodic peaks. Because of the difficult solid-state diffusion at higher rates, the pseudo-capacitance becomes even prominent especially at 50 C under the fast surface kinetics.

Discussion

The Fe$_2$O$_3$ nanomembrane electrodes in this work demonstrate ultra-long and stable cycling life at high rates with satisfactory capacity (808 mAh g^{-1} after 1000 cycles at 2 C and 530 mAh g^{-1} after 3000 cycles at 6 C) as well as high rate capability up to 50 C with the capacity of 178 mAh g^{-1}. There are several reasons responsible for the excellent electrochemical performance. As mentioned in the introduction, nanostructures for applications in LIBs have large electrode/electrolyte surface contact area for interfacial storage, nano-sized diffusion paths for Li$^+$, and better alleviation of volume expansion during cycling. Like other forms of nanostructured Fe$_2$O$_3$, the Fe$_2$O$_3$ nanomembranes also have these common structural merits of nanostructures. However, the excellent electrochemical performance is preferably believed to benefit more from the structural advantages of the two-dimensional nanomembranes.

The unique mechanical feature of the nanomembranes to wrinkle and bend can effectively buffer the strain of lithiation/delithiation, which can be evidenced by the SEM images of the Fe_2O_3 nanomembranes before and after cycling at 2 C. Before cycling, the parallel-laid planar nanomembranes can be seen from Supplementary Fig. S4a and S4b with the thickness of about 103 ~ 165 nm. After the first cycle (Supplementary Fig. S4c and S4d), most of the nanomembranes are still relatively planar with increased thickness of ~224 nm due to the SEI layer formation. After 250 cycles (Supplementary Fig. S4e and S4f), although much wrinkled under the strain of repeated lithiation/delithiation, the thickened nanomembranes (thickness of ~302 nm) with thicker SEI layer still maintain the layer structure with high integrity instead of pulverization. The good mechanical stability enables the nanomembranes to extend the cycling life by postponing pulverization. In addition, the nanomembranes can provide two-dimensional transport pathways in between the layers to promote the pseudo-capacitive type storage[9]. Therefore, once the SEI layer and the polymeric gel-like film are formed, the parallel-laid nanomembranes with the electrolyte filled in between the layers electrochemically act like numerous "mini-capacitors" to provide excess capacity in the form of the pseudo-capacitance. At high current rate with difficult solid-state diffusion of Li^+, the pseudo-capacitance will be more prominent to maintain the capacity thus enabling the long cycling life. This contribution shows great potential of 2D nanomembrane structured electrode materials in extending the cycling life and improving rate capability for high power batteries.

Methods

Fabrication of free-standing Fe_2O_3 nanomembranes. The free-standing Fe_2O_3 nanomembranes are fabricated by a peel-off strategy with Al_2O_3 film as sacrificial layer together with thermal treatment. Typically, a 100 nm Al_2O_3 film as sacrificial layer and a 50 nm Fe nanomembrane were sequentially deposited onto the glass slide substrate by e-beam deposition (BOC Edwards FL400) with bulk Fe source (Kurt J. Lesker). The thickness of the deposited film was controlled by a quartz crystal microbalance, and the tooling factor was calibrated by depositing a 200 nm film, the actual thickness of which was then measured by a Profilometer Dektak XT (Brucker). Free-standing Fe nanomembranes were obtained by etching away the Al_2O_3 sacrificial layer with 4 mol L^{-1} NaOH aqueous solution (100 °C)[49]. The Fe nanomembranes were then repeatedly filtered and washed with distilled water, ethanol, and acetone for several times respectively, and then dried in a critical point dryer (CPD). Finally, the Fe_2O_3 nanomembranes were obtain by annealing the Fe nanomembranes in a muffle furnace at 450 °C for 3 h in atmosphere.

Characterizations. The morphology of the free-standing Fe_2O_3 nanomembranes was inspected by scanning electron microscopy (SEM) DSM 982, Zeiss. Focused ion beam (FIB) etching for thickness measurements was performed by a scanning electron microscopy (SEM) NVision 40 CrossBeam, Carl Zeiss. The crystallinity and composition of the sample were determined by X-ray diffraction (XRD) diffractometer, PANalytical X'Pert PRO Diffraction, Co-Kα radiation, reflection geometry. Raman spectroscopy (Renishaw) was performed at a 442 nm wavelength to identify the composition. The oxidation state of the sample was identified by X-ray photoelectron spectroscopy (PHI 5600 CI, using monochromatic Al-Kα radiation for excitation, 350 W). The microstructure and lattice fringes were observed with HAADF-STEM, FEI Titan ChemiSTEM 80-200.

Electrochemical measurements. Electrochemical measurements were performed with two-electrode Swagelok-type half-cells assembled in an Ar-filled glove box (H_2O, O_2<0.1 ppm, Mbraun, Germany). To prepare the working electrodes, the Fe_2O_3 nanomembranes were mixed and ground with conductive additive carbon black (Timcal) and sodium alginate (Aldrich) binder at a weight ratio of 7 : 2 : 1 in water, and then the obtained paste was coated onto a Cu foil (Goodfellow) current collector and finally dried at 60 °C for 10 h in vacuum oven. The areal density of the active electrode material in the electrodes was determined to be 0.59 ~ 0.63 mg cm^{-2}. The electrode plate was punched into several discs with ϕ=10 mm for batteries assembly. The battery was assembled with a punched electrode disc as the working electrode, a Li foil (ϕ=10 mm) as the counter/reference electrode, a glass fiber membrane (Whatman) as the separator, and the solution of 1 mol L^{-1} $LiPF_6$ in ethylene carbonate/dimethyl carbonate/diethyl carbonate (1 : 1 : 1, wt. %, Merck) including 2 vol. % vinylene carbonate (Merck) additive as the electrolyte. Galvanostatic discharge/charge cycling was performed with a multichannel battery testing system (Arbin BT 2000) within 0.01 ~ 3.0 V vs. Li/Li^+ at different current densities. The cyclic voltammetry (CV) at a scan rate of 0.1 mV s^{-1} within 0.003 ~ 3.0 V vs. Li/Li^+ as well as the electrochemical impedance spectra (EIS) from 100 kHz to 500 µHz with a perturbation voltage of 10 mV were performed on Zahner electrochemical workstation (IM6) at room temperature.

1. Huang, G. S. & Mei, Y. F. Thinning and shaping solid films into functional and integrative nanomembranes. *Adv. Mater.* **24**, 2517–2546 (2012).
2. Rogers, J. A., Lagally, M. G. & Nuzzo, R. G. Synthesis, assembly and applications of semiconductor nanomembranes. *Nature* **477**, 45–53 (2011).
3. Nikoobakht, B. & Li, X. L. Two-dimensional nanomembranes: Can they outperform lower dimensional nanocrystals? *ACS Nano* **6**, 1883–1887 (2012).
4. Schmidt, O. G. & Eberl, K. Nanotechnology: Thin solid films roll up into nanotubes. *Nature* **410**, 168–168 (2001).
5. Kim, D. H. & Rogers, J. A. Bend, buckle, and fold: Mechanical engineering with nanomembranes. *ACS Nano* **3**, 498–501 (2009).
6. Deng, J. et al. Naturally rolled-up C/Si/C trilayer nanomembranes as stable anodes for lithium-ion batteries with remarkable cycling performance. *Angew. Chem., Int. Ed.* **52**, 2326–2330 (2013).
7. Zhang, L. et al. Hierarchically designed SiO_x/SiO_y bilayer nanomembranes as stable anodes for lithium ion batteries. *Adv. Mater.* **26**, 4527–4532 (2014).
8. Bufon, C. C. B. et al. Self-assembled ultra-compact energy storage elements based on hybrid nanomembranes. *Nano Lett.* **10**, 2506–2510 (2010).
9. Augustyn, V. et al. High-rate electrochemical energy storage through Li^+ intercalation pseudocapacitance. *Nat. Mater.* **12**, 518–522 (2013).
10. Tarascon, J. M. & Armand, M. Issues and challenges facing rechargeable lithium batteries. *Nature* **414**, 359–367 (2001).
11. Armand, M. & Tarascon, J. M. Building better batteries. *Nature* **451**, 652–657 (2008).
12. Goodenough, J. B. & Kim, Y. Challenges for rechargeable Li batteries. *Chem. Mater.* **22**, 587–603 (2010).
13. Bruce, P. G., Scrosati, B. & Tarascon, J. M. Nanomaterials for Rechargeable Lithium Batteries. *Angew. Chem. Int. Edit.* **47**, 2930–2946 (2008).
14. Ji, L. W., Lin, Z., Alcoutlabi, M. & Zhang, X. W. Recent developments in nanostructured anode materials for rechargeable lithium-ion batteries. *Energy Environ. Sci.* **4**, 2682–2699 (2011).
15. Arico, A. S., Bruce, P., Scrosati, B., Tarascon, J. M. & Van Schalkwijk, W. Nanostructured materials for advanced energy conversion and storage devices. *Nat. Mater.* **4**, 366–377 (2005).
16. Guo, Y. G., Hu, J. S. & Wan, L. J. Nanostructured materials for electrochemical energy conversion and storage devices. *Adv. Mater.* **20**, 2878–2887 (2008).
17. Lin, Y. M., Abel, P. R., Heller, A. & Mullins, C. B. α-Fe_2O_3 nanorods as anode material for lithium ion batteries. *J. Phys. Chem. Lett.* **2**, 2885–2891 (2011).
18. Chen, J., Xu, L. N., Li, W. Y. & Gou, X. L. α-Fe_2O_3 nanotubes in gas sensor and lithium-ion battery applications. *Adv. Mater.* **17**, 582–586 (2005).
19. Zhang, L., Wu, H. B., Madhavi, S., Hng, H. H. & Lou, X. W. Formation of Fe_2O_3 microboxes with hierarchical shell structures from metal-organic frameworks and their lithium storage properties. *J. Am. Chem. Soc.* **134**, 17388–17391 (2012).
20. Xu, S. et al. α-Fe_2O_3 multi-shelled hollow microspheres for lithium ion battery anodes with superior capacity and charge retention. *Energy Environ. Sci.* **7**, 632–637 (2014).
21. Zhu, J. X. et al. Hierarchical hollow spheres composed of ultrathin Fe_2O_3 nanosheets for lithium storage and photocatalytic water oxidation. *Energy Environ. Sci.* **6**, 987–993 (2013).
22. Wang, Z. Y., Luan, D. Y., Madhavi, S., Hu, Y. & Lou, X. W. Assembling carbon-coated α-Fe_2O_3 hollow nanohorns on the CNT backbone for superior lithium storage capability. *Energy Environ. Sci.* **5**, 5252–5256 (2012).
23. Kan, J. & Wang, Y. Large and fast reversible Li-ion storages in Fe_2O_3-graphene sheet-on-sheet sandwich-like nanocomposites. *Sci. Rep.* **3**, 3502 (2013).
24. Yang, S. B. et al. Porous iron oxide ribbons grown on graphene for high-performance lithium storage. *Sci. Rep.* **2** (2012).
25. Davenport, A. J., Oblonsky, L. J., Ryan, M. P. & Toney, M. F. The structure of the passive film that forms on iron in aqueous environments. *J. Electrochem. Soc.* **147**, 2162–2173 (2000).
26. Ogrady, W. E. Mössbauer study of the passive oxide film on iron. *J. Electrochem. Soc.* **127**, 555–563 (1980).
27. Amaral, S. T., Martini, E. M. A. & Muller, I. L. An attempt of experimental separation of the potentiodynamic anodic peaks of iron in alkaline solutions and application of the ohmic model for passive film growth. *Corros. Sci.* **43**, 853–879 (2001).
28. Shim, S. H. & Duffy, T. S. Raman spectroscopy of Fe_2O_3 to 62 GPa. *Am. Mineral.* **87**, 318–326 (2002).
29. de Faria, D. L. A., Silva, S. V. & de Oliveira, M. T. Raman microspectroscopy of some iron oxides and oxyhydroxides. *J. Raman Spectrosc.* **28**, 873–878 (1997).
30. Jubb, A. M. & Allen, H. C. Vibrational spectroscopic characterization of hematite, maghemite, and magnetite thin films produced by vapor deposition. *ACS Appl. Mater. Interfaces* **2**, 2804–2812 (2010).
31. Bersani, D., Lottici, P. P. & Montenero, A. Micro-Raman investigation of iron oxide films and powders produced by sol-gel syntheses. *J. Raman Spectrosc.* **30**, 355–360 (1999).
32. Muruganandham, M. et al. Facile fabrication of hierarchical α-Fe_2O_3: Self-assembly and its magnetic and electrochemical properties. *J. Phys. Chem. C* **115**, 18164–18173 (2011).

33. Larcher, D. *et al.* Combined XRD, EXAFS, and Mössbauer studies of the reduction by lithium of α-Fe_2O_3 with various particle sizes. *J. Electrochem. Soc.* **150**, A1643–A1650 (2003).

34. Kanzaki, S. *et al.* Nano-sized γ-Fe_2O_3 as lithium battery cathode. *J. Power Sources* **146**, 323–326 (2005).

35. Laruelle, S. *et al.* On the origin of the extra electrochemical capacity displayed by MO/Li cells at low potential. *J. Electrochem. Soc.* **149**, A627–A634 (2002).

36. Morales, J., Sanchez, L., Martin, F., Berry, F. & Ren, X. L. Synthesis and characterization of nanometric iron and iron-titanium oxides by mechanical milling: Electrochemical properties as anodic materials in lithium cells. *J. Electrochem. Soc.* **152**, A1748–A1754 (2005).

37. Jiang, Y. *et al.* Amorphous Fe_2O_3 as a high-capacity, high-rate and long-life anode material for lithium ion batteries. *Nano Energy* **4**, 23–30 (2014).

38. Shin, J. Y., Samuelis, D. & Maier, J. Sustained lithium-storage performance of hierarchical, nanoporous anatase TiO_2 at high rates: Emphasis on interfacial storage phenomena. *Adv. Funct. Mater.* **21**, 3464–3472 (2011).

39. Jamnik, J. & Maier, J. Nanocrystallinity effects in lithium battery materials - Aspects of nano-ionics. Part IV. *Phys. Chem. Chem. Phys.* **5**, 5215–5220 (2003).

40. Balaya, P., Li, H., Kienle, L. & Maier, J. Fully reversible homogeneous and heterogeneous Li storage in RuO_2 with high capacity. *Adv. Funct. Mater.* **13**, 621–625 (2003).

41. Hu, Y. Y. *et al.* Origin of additional capacities in metal oxide lithium-ion battery electrodes. *Nat. Mater.* **12**, 1130–1136 (2013).

42. Park, M., Zhang, X. C., Chung, M. D., Less, G. B. & Sastry, A. M. A review of conduction phenomena in Li-ion batteries. *J. Power Sources* **195**, 7904–7929 (2010).

43. Yu, P., Ritter, J. A., White, R. E. & Popov, B. N. Ni-composite microencapsulated graphite as the negative electrode in lithium-ion batteries - II. Electrochemical impedance and self-discharge studies. *J. Electrochem. Soc.* **147**, 2081–2085 (2000).

44. Haran, B. S., Popov, B. N. & White, R. E. Determination of the hydrogen diffusion coefficient in metal hydrides by impedance spectroscopy. *J. Power Sources* **75**, 56–63 (1998).

45. Yu, P., Popov, B. N., Ritter, J. A. & White, R. E. Determination of the lithium ion diffusion coefficient in graphite. *J. Electrochem. Soc.* **146**, 8–14 (1999).

46. Duan, W. *et al.* $Na_3V_2(PO_4)_3$@C core-shell nanocomposites for rechargeable sodium-ion batteries *J. Mater. Chem. A* (2014).

47. Taberna, P. L., Simon, P. & Fauvarque, J. F. Electrochemical characteristics and impedance spectroscopy studies of carbon-carbon supercapacitors. *J. Electrochem. Soc.* **150**, A292–A300 (2003).

48. Si, W. P. *et al.* On chip, all solid-state and flexible micro-supercapacitors with high performance based on MnOx/Au multilayers. *Energy Environ. Sci.* **6**, 3218–3223 (2013).

49. Zhao, S., Roberge, H., Yelon, A. & Veres, T. New application of AAO template: A mold for nanoring and nanocone arrays. *J. Am. Chem. Soc.* **128**, 12352–12353 (2006).

Author contributions

X.L., C.Y. and O.G.S. devised the original concept. X.L. performed the material fabrication, Raman, SEM, and electrochemical measurements. S.B. did FIB cutting, S.O. performed XPS analysis, and L.L. performed TEM. X.L. analyzed the data, made the graphs and wrote the manuscript (J.Z. wrote the introduction). W.S., J.Z., X.S., J.D., S.B. and C.Y. contributed to the discussion. All authors reviewed the manuscript.

Additional information

Supplementary information accompanies this paper at http://www.nature.com/scientificreports

Competing financial interests: The authors declare no competing financial interests.

How to cite this article: Liu, X. *et al.* Free-standing Fe_2O_3 nanomembranes enabling ultra-long cycling life and high rate capability for Li-ion batteries. *Sci. Rep.* **4**, 7452; DOI:10.1038/srep07452 (2014).